INTERNATIONAL JOURNAL FOR NUMERICAL METHODS IN FLUIDS
Int. J. Numer. Meth. Fluids 2001; **36**: 619–637 (DOI: 10.1002/fld.144)

Incompressible flows with combustion simulated by a preconditioning method using multigrid acceleration and MUSCL reconstruction

V. Bellucci[a,1] and C. Bruno[b,*,2]

[a] *CRS4 Research Centre, C.P. 94, I-09010 Uta (CA), Italy*
[b] *Dip. Meccanica & Aeronautica, Università di Roma I, Via Eudossiana 18, I-00184 Rome, Italy*

SUMMARY

A numerical algorithm for the steady state solution of three-dimensional incompressible flows is presented. A preconditioned time marching scheme is applied to the conservative form of the governing equations. The preconditioning matrix multiplies the time derivatives of the system and circumvents the eigenvalue-caused stiffness at low speed. The formulation is suitable for constant density flows and for flows where the density depends on non-passive scalars, such as in low-speed combustion applications. The $k-\varepsilon$ model accounts for turbulent transport effects. A cell-centred finite volume formulation with a Runge–Kutta time stepping scheme for the primitive variables is used. Second-order spatial accuracy is achieved by developing for the preconditioned system an approximate Riemann solver with MUSCL reconstruction. A multi-grid technique coupled with local time stepping and implicit residual smoothing is used to accelerate the convergence to the steady state solution. The convergence behaviour and the validation of the predicted solutions are examined for laminar and turbulent constant density flows and for a turbulent non-premixed flame simulated by a presumed probability density function (PDF) model.

KEY WORDS: combustion; incompressible flow; multigrid; preconditioning methods

1. INTRODUCTION

Computational fluid dynamics (CFD) is extensively used to simulate industrially important physical problems in the low Mach number regime, where the incompressibility condition (i.e. density no longer related to pressure fluctuations) is a valid assumption. Incompressible flows

* Correspondence to: Dip. Meccanica & Aeronautica, Università di Roma I, Via Eudossiana 18, I-00184 Rome, Italy.
[1] E-mail: bellucci@crs4.it
[2] E-mail: c.bruno@dma.uniroma1.it

Received May 1999
Revised October 1999

may be both non-reacting flows at low speed (where the density is assumed to be constant) or, as in many combustion applications, such as gas turbines, combustor chamber flows, where density is assumed to depend only on heat release [1].

Historically, pressure-based approaches were dominant in the early days of the simulation of incompressible flows. In these methods, pressure is either updated by a Poisson equation or by a correction equation obtained from the continuity equation acting as a constraint condition for the momentum field [2,3].

On the other hand, time marching density based codes have been successfully used for a wide range of Mach numbers where compressibility is important. These codes have become highly sophisticated in terms of geometry complexity, accurate spatial discretization and convergence acceleration techniques. Unfortunately, numerical algorithms developed for compressible flows are often ineffective when the Mach number becomes of the order of that found in typical aero-engine combustion chambers [$\sim \mathcal{O}(10^{-3})$] because of the stiffness of the system's eigenvalues. Actually, the time step of explicit schemes is limited for stability reasons and the maximum allowable time step is inversely proportional to the largest eigenvalue, which for low speeds is approximately the speed of sound. However, the time step associated with the waves convected at the fluid speed approaches infinity as the Mach number approaches zero. Hence, the convergence slows dramatically due to the disparity of the wave speeds. Further difficulties are present if the flow is assumed incompressible (because pressure cannot be updated by using the equation of state) and in combustion simulations (where strong density changes occur due to heat release).

In recent years preconditioning methods have been used to eliminate the eigenvalues stiffness at low speed. The major advantage of the preconditioning methods is that they may be easily implemented into existing time marching compressible codes, whose features are retained. These methods are based on the technique developed by Chorin [4]: an artificial compressibility term in the form of a time derivative of pressure replaces the time derivative of density in the continuity equation. Different methods based on the artificial compressibility technique have been suggested. A perturbed form of the governing equations may be obtained by expanding the flow variables in terms of the Mach number. Low-speed flows with volumetric heat addition have been simulated by employing such techniques [5]. Alternatively, a suitable preconditioning matrix may be introduced. The preconditioning matrix premultiplies the time derivatives of the system and rescales the eigenvalues to the same order of magnitude. Preconditioning matrices have been proposed for incompressible and compressible flows [6–8]. Recently, this preconditioning approach has been proposed to solve reacting and non-reacting flows within a wide Mach number range [9–11].

The objective of this paper is to employ a preconditioning technique based on the use of a preconditioning matrix to simulate incompressible flows, where the density is constant or depends only on some integrated scalars, such as temperature or chemical species' mass fractions. An MUSCL scheme for the discretization of the inviscid fluxes and a multi-grid technique are developed for the preconditioned system of equations. Numerical simulations of laminar and turbulent internal flows, as well as a turbulent diffusion flame modelled by assumed probability density function (PDF) is presented.

2. GOVERNING EQUATIONS

The continuity, momentum and non-passive scalar equations are expressed as [1]

$$\frac{\partial \bar{\rho}}{\partial t} + \nabla\cdot(\bar{\rho}\tilde{\mathbf{u}}) = 0 \tag{1}$$

$$\frac{\partial \bar{\rho}\tilde{\mathbf{u}}}{\partial t} + \nabla\cdot(\bar{\rho}\tilde{\mathbf{u}}\tilde{\mathbf{u}}) + \nabla\bar{p} = \nabla\cdot\boldsymbol{\tau} \tag{2}$$

$$\frac{\partial \bar{\rho}\tilde{\phi}_\ell}{\partial t} + \nabla\cdot(\bar{\rho}\tilde{\phi}_\ell\tilde{\mathbf{u}}) = \nabla\cdot(D_\ell\nabla\tilde{\phi}_\ell) + H_\ell \tag{3}$$

where the overbar is the Reynolds averaging operator, the overtilde is the Favre averaging operator, t is the time, ρ is the density, $\mathbf{u}$ is the velocity vector, p is the pressure, ϕ_ℓ is the non-passive scalar ($\ell = 1, N_s$, N_s being the number of integrated scalars), D_ℓ is the non-passive scalar diffusion coefficient and H_ℓ is the non-passive scalar source term. Turbulence effects are accounted for by integrating the two k–ε model scalar equations

$$\frac{\partial \bar{\rho}k}{\partial t} + \nabla\cdot(\bar{\rho}k\tilde{\mathbf{u}}) = \nabla\cdot\left[\left(\frac{\mu+\mu_t}{\sigma_k}\right)\nabla k\right] + \mathscr{P} - \bar{\rho}\varepsilon \tag{4}$$

$$\frac{\partial \bar{\rho}\varepsilon}{\partial t} + \nabla\cdot(\bar{\rho}\varepsilon\tilde{\mathbf{u}}) = \nabla\cdot\left[\left(\frac{\mu+\mu_t}{\sigma_\varepsilon}\right)\nabla\varepsilon\right] + \frac{\varepsilon}{k}(c_1\mathscr{P} - c_2\bar{\rho}\varepsilon) \tag{5}$$

where k is the turbulence kinetic energy, ε is the turbulence dissipation rate, μ is the laminar viscosity and μ_t is the turbulent viscosity. The stress tensor τ is given by

$$\tau = (\mu+\mu_t)(\nabla\tilde{\mathbf{u}} + \nabla\tilde{\mathbf{u}}^T) - \frac{2}{3}[(\mu+\mu_t)(\nabla\cdot\tilde{\mathbf{u}}) + \tilde{\rho}k]\mathbf{I} \tag{6}$$

where $\mathbf{I}$ is the unit tensor. The turbulent viscosity μ_t and the turbulence production term $\mathscr{P}$ are expressed respectively as

$$\mu_t = c_\mu\frac{\bar{\rho}k^2}{\varepsilon} \tag{7}$$

$$\mathscr{P} = \mu_t(\nabla\tilde{\mathbf{u}} + \nabla\tilde{\mathbf{u}}^T)\colon\nabla\tilde{\mathbf{u}} - \frac{2}{3}[\mu_t(\nabla\cdot\tilde{\mathbf{u}}) + \bar{\rho}k](\nabla\cdot\tilde{\mathbf{u}}) \tag{8}$$

According to the 'standard' k–ε model, the following values are assigned to the turbulence constants: $\sigma_k = 1$, $\sigma_\varepsilon = 1.3$, $c_1 = 1.45$, $c_2 = 1.92$ and $c_\mu = 0.09$.

By assuming a constant laminar viscosity and constant laminar diffusion coefficients, the system of governing equations (1)–(3) is closed by the equation of state

$$\bar{\rho} = \bar{\rho}(\phi_\ell) \tag{9}$$

2.1. Non-premixed turbulent combustion model

The non-passive scalar case we consider is that of a turbulent diffusion flame. Following the conserved scalar approach [13], a diffusion flame may be simulated by integrating the two scalar equations

$$\frac{\partial \bar{\rho}\tilde{f}}{\partial t} + \nabla\cdot(\bar{\rho}\tilde{f}\tilde{\mathbf{u}}) = \nabla\cdot(D\nabla\tilde{f}) \tag{10}$$

$$\frac{\partial \bar{\rho}\widetilde{f''^2}}{\partial t} + \nabla\cdot(\bar{\rho}\widetilde{f''^2}\tilde{\mathbf{u}}) = \nabla\cdot(D\nabla\widetilde{f''^2}) + 2\frac{\mu_t}{Pr_t}\nabla\tilde{f}\cdot\nabla\tilde{f} - c_f\bar{\rho}\frac{\varepsilon}{k}\widetilde{f''^2} \tag{11}$$

where f is the mixture fraction, f''^2 is the mixture fraction variance and $c_f = 1$. The diffusion coefficient D is given by

$$D = \frac{\mu}{Pr} + \frac{\mu_t}{Pr_t} \tag{12}$$

where $Pr = 0.7$ and $Pr_t = 0.7$ are the laminar and turbulent Prandtl number respectively.

The assumptions that lead to the conserved scalar model are: two-feed flow (and uniform composition and temperature in the two feeds); a low Mach number; Dufour and Soret effects neglected; species specific heats at constant pressure assumed constant; equal diffusion coefficient for all the species; Lewis number equal to one; adiabatic walls; body forces and radiative flux neglected. The conserved scalar f represents either the normalized non-averaged enthalpy $(h - h_2)/(h_1 - h_2)$ or the mixture fraction (e.g. the mass fraction of material in the mixture originated in feed 1, with $(1 - f)$ originated in feed 2) [13]. The variance $\widetilde{f''^2}$ accounts for the fluctuations of $\tilde{f}$ due to turbulence. Under thermochemical equilibrium and low Mach number hypothesis, the density is assumed to be a function of f alone, expressed as

$$\rho = \frac{p_0}{F(f)} \tag{13}$$

where p_0 is the combustor average pressure. The function $F(f)$ (depending on the equilibrium chemistry between a specific fuel and air) is approximated by the N-polynomial fit

$$F(f) = \sum_{n=0}^{N} c_n f^n \tag{14}$$

obtained by minimizing the Gibbs free energy of the products mixture [14]. The mean density is evaluated by

$$\bar{\rho} = \left[\int_0^1 \frac{\tilde{P}(f)}{\rho(f)} \, \mathrm{d}f \right]^{-1} = p_0 \left[\int_0^1 F(f) \tilde{P}(f) \, \mathrm{d}f \right]^{-1} \tag{15}$$

where $\tilde{P}(f)$ is the Favre probability density function. Using the assumed β-PDF model [15], $\tilde{P}(f)$ is given by

$$\tilde{P}(f) = \frac{f^{a-1}(1-f^{b-1})}{\int_0^1 f^{a-1}(1-f^{b-1}) \, \mathrm{d}f} \tag{16}$$

where

$$a = \frac{\tilde{f}^2(1-\tilde{f})}{\widetilde{f''^2}} - \tilde{f}, \qquad b = \frac{\tilde{f}^2(1-\tilde{f})^2}{\widetilde{f''^2}} - (1-\tilde{f})$$

By substituting Equations (14) and (16) in Equation (15) one has

$$\bar{\rho} = \frac{p_0 A_0}{\sum_{n=0}^{N} c_n A_n} \tag{17}$$

where the integrals A_n are expressed as [16]

$$A_n = \int_0^1 f^{a-1+n}(1-f^{b-1}) \, \mathrm{d}f = A_0 \prod_{m=1}^{n} \frac{a-1+m}{a+b-1+m} \tag{18}$$

3. PRECONDITIONING METHOD

Following the cell-centred finite volume approach, the system of governing equations (1)–(3) can be written in compact form as

$$\frac{\mathrm{d}\mathbf{W}}{\mathrm{d}t} = -\frac{1}{\Omega} \sum_m [(\mathbf{F}_E - \mathbf{F}_V) \cdot \mathbf{n}]_m S_m + \mathbf{H} \tag{19}$$

where $\mathbf{W} = [\bar{\rho}, \bar{\rho}\tilde{\mathbf{u}}, \bar{\rho}\tilde{\phi}_\ell]^T$ is the conserved variables vector with $\tilde{\phi}_\ell = (k, \varepsilon, \tilde{f}, \widetilde{f''^2})$. Furthermore, Ω is the cell volume, $\mathbf{F}_E$ is the inviscid flux, $\mathbf{F}_V$ is the viscous flux, S_m is the area of the m-interface of the cell and $\mathbf{H}$ is the source term vector.

As noted, time marching algorithms applied to Equation (19) become ineffective at low speed because of eigenvalue stiffness. Furthermore, in Equation (19) the pressure cannot be numerically updated by the equation of state (9). This problem is circumvented by using the following preconditioning technique: by introducing the matrix

$$\mathbf{K} = \begin{bmatrix} 1 & 0 & 0 \\ -\tilde{\mathbf{u}} & \mathbf{I} & 0 \\ -\tilde{\phi}_\ell & 0 & \mathbf{I} \end{bmatrix} \tag{20}$$

Equation (19) is transformed to the non-conservative form

$$\left(\mathbf{K}\frac{\partial \mathbf{W}}{\partial \mathbf{Q}}\right)\frac{\mathrm{d}\mathbf{Q}}{\mathrm{d}t} = -\frac{1}{\Omega}\mathbf{K}\sum_m [(\mathbf{F}_E - \mathbf{F}_V)\cdot\mathbf{n}]_m S_m + \mathbf{K}\mathbf{H} \tag{21}$$

in terms of the primitive variables vector $\mathbf{Q} = [(P - p_0), \tilde{\mathbf{u}}, \tilde{\phi}_\ell]^T$. The integrated variable $(P - p_0)$ eliminates the round-off error arising in the computation of pressure and pressure gradients. In the matrix

$$\mathbf{K}\frac{\partial \mathbf{W}}{\partial \mathbf{Q}} = \begin{bmatrix} 0 & 0 & \bar{\rho}_{\tilde{\phi}_\ell} \\ 0 & \bar{\rho}\mathbf{I} & 0 \\ 0 & 0 & \bar{\rho}\mathbf{I} \end{bmatrix} \tag{22}$$

the term (1, 1), which multiplies the time derivative of pressure, controls the pressure wave speeds and is responsible for the eigenvalues' stiffness. The stiffness is avoided by replacing the matrix (22) with matrix [6]

$$\mathbf{P}^{-1} = \begin{bmatrix} \dfrac{1}{\beta} & 0 & 0 \\ 0 & \bar{\rho}\mathbf{I} & 0 \\ 0 & 0 & \bar{\rho}\mathbf{I} \end{bmatrix} \tag{23}$$

where β represents the pressure wave speed of the preconditioned system. Therefore, Equation (21) is replaced by

$$\frac{\mathrm{d}\mathbf{Q}}{\mathrm{d}t} = -\frac{1}{\Omega}\mathbf{\Gamma}\sum_m [(\mathbf{F}_E - \mathbf{F}_V)\cdot\mathbf{n}]_m S_m + \mathbf{\Gamma}\mathbf{H} \tag{24}$$

where the preconditioning matrix $\mathbf{\Gamma}$ is defined as

$$\mathbf{\Gamma} = \mathbf{P}\mathbf{K} = \begin{bmatrix} \beta & 0 & 0 \\ -\dfrac{\tilde{u}}{\bar{\rho}} & \dfrac{\mathbf{I}}{\bar{\rho}} & 0 \\ -\dfrac{\tilde{\phi}_\ell}{\bar{\rho}} & 0 & \dfrac{\mathbf{I}}{\bar{\rho}} \end{bmatrix} \tag{25}$$

In Equation (24), pressure is updated by its time derivative and the equation of state is employed to obtain the density. For constant density flows the preconditioning reduces to the artificial compressibility method of Chorin [4]. Otherwise, the method is an extension of the artificial compressibility method to flows where the density depends on non-passive scalars.

By defining the inviscid numerical flux as $f = \mathbf{F}_E \cdot \mathbf{n}$ ($\mathbf{n}$ being the normal to the cell interface), the eigenvalues of the preconditioned inviscid Jacobian $\mathbf{A} = \boldsymbol{\Gamma} \partial \mathbf{f} / \partial \mathbf{Q}$ are

$$\lambda_r(\mathbf{A}) = U,\ U,\ U,\ U/2 + c,\ U/2 - c \tag{26}$$

where $U = \tilde{\mathbf{u}} \cdot \mathbf{n}$ is the contravariant velocity and $c = \sqrt{(U/2)^2 + \beta}$ is the pseudo-speed of sound. In this work β is given by $\beta = \beta_0 U_\infty^2$, where U_∞ is a free-stream velocity and β_0 is a constant greater than zero in order to ensure that one eigenvalue is negative for subsonic flows. The value of β is critical for the convergence properties of the method. Actually, well-conditioned λ_r are obtained when β makes the pseudo-acoustic wave speed of the same order as the particle velocity (i.e. $\beta_0 = 1$). Nevertheless, when the Reynolds number decreases, the characteristic time of viscosity spreading also decreases, and if β is too small, the boundary layer cannot adapt to the too-slowly developing pressure field and fluctuations of separation regions may destroy the convergence [7]. Numerical experiments reported below will illustrate the influence of β on the properties of the numerical scheme.

4. SOLUTION PROCEDURE

Roe's approximate Riemann solver [17] is used for the spatial discretization of inviscid fluxes. At the interface $(i + 1/2)$ between the adjacent cells (i, j, k) and $(i + 1, j, k)$, $\mathbf{f}_{i+1/2}$ is evaluated by using the expression

$$\mathbf{f}_{i+1/2} = \frac{\mathbf{f}_\mathrm{L} + \mathbf{f}_\mathrm{R}}{2} - \frac{1}{2} \boldsymbol{\Gamma}^{-1} |\mathbf{A}_{i+1/2}| \Delta \mathbf{Q} \tag{27}$$

where $\Delta(\cdot) = (\cdot)_\mathrm{R} - (\cdot)_\mathrm{L}$ and where the left and right states $\mathbf{Q}_\mathrm{L}$ and $\mathbf{Q}_\mathrm{R}$ are computed by extending the MUSCL approach of Reference [18] to the preconditioned system. It yields

$$\mathbf{Q}_\mathrm{R} = \mathbf{Q}_{i+1} - \frac{1}{2} \overline{\overline{\Delta \mathbf{Q}}}_{i+3/2} \tag{28}$$

$$\mathbf{Q}_\mathrm{L} = \mathbf{Q}_i + \frac{1}{2} \overline{\overline{\Delta \mathbf{Q}}}_{i+1/2} \tag{29}$$

where spurious oscillations are eliminated using

$$\overline{\overline{\Delta \mathbf{Q}}}_{i+1/2} = \mathrm{minmod}[\Delta \mathbf{Q}_i,\ \omega(\Delta \mathbf{Q}_{i-1})] \tag{30}$$

with

$$\Delta\mathbf{Q}_i = \mathbf{Q}_{i+1} - \mathbf{Q}_i$$

$$\text{minmod}(x, y) = \text{sgn}(x) \cdot \max\{0, \min[|x|, y\ \text{sgn}(x)]\}$$

The value $\omega = 1$ (second-order full-upwind scheme) is employed for all the equations apart from the k–ε equations (4) and (5), for which $\omega = 0$ (first-order upwind scheme). The first-order upwind discretization of k–ε equations increases the robustness of the solver and is justified by the fact that, for combustion applications, viscous terms are dominant in turbulence equations [1]. In Equation (27) $|\mathbf{A}| = \mathbf{R}|\mathbf{\Lambda}|\mathbf{R}^{-1}$, where $\mathbf{R}$ is the matrix of inviscid right eigenvectors, $|\mathbf{\Lambda}| = \text{diag}(|\lambda_r|)$ and arithmetic averaging between $\mathbf{Q}_\text{R}$ and $\mathbf{Q}_\text{L}$ is used to define the interface values. After rearranging terms, one has

$$|\mathbf{A}|\Delta\mathbf{Q} = \begin{bmatrix} \beta\left(\dfrac{\Delta\bar{p}}{c} + M\delta\right) \\ M\dfrac{\Delta\bar{p}}{\bar{\rho}}\,\mathbf{n} + |U|\Delta\tilde{\mathbf{u}} + C\dfrac{\delta}{\bar{\rho}}\,\mathbf{n} \\ |U|\Delta\tilde{\phi}_l \end{bmatrix} \tag{31}$$

where

$$\delta = \bar{\rho}\,\Delta U + U\Delta\bar{\rho}$$

$$C = c(1 + M^2) - |U|$$

and $M = (U/2)/c$ is the pseudo-Mach number.

The discretization of the viscous terms is obtained by using a discrete form of the Gauss theorem, leading to a central approximation of the viscous fluxes [19]. The time integration is performed by a five-stage Runge–Kutta algorithm applied to the set of coupled ordinary differential equations (24) written in the form

$$\Omega\frac{\mathrm{d}\mathbf{Q}}{\mathrm{d}t} = \mathscr{R}(\mathbf{Q}) \tag{32}$$

where $\mathscr{R}$ is the preconditioned residual. The Runge–Kutta scheme convergence is accelerated by local time stepping and implicitly smoothing. In the local time stepping procedure, the equation is advanced in time by the maximum time step in each mesh cell. The local time step is calculated by considering stability limitations due to both the convective and the viscous eigenvalues of the system. The stability range of the time integration scheme is increased by implicitly smoothing the residuals at each stage. The right-hand side residual $\mathscr{R}$ of Equation (32) is thus replaced by the average $\overline{\overline{\mathscr{R}}}$ of itself and the neighbouring residuals, following the expression

$$(1 - \sigma\nabla_k^2)(1 - \sigma\nabla_j^2)(1 - \sigma\nabla_i^2)\overline{\overline{\mathscr{R}}} = \mathscr{R} \tag{33}$$

where ∇_i^2 is the second-order central differencing in the i-direction and $\sigma = 0.5$ is used in all the computations.

4.1. Multi-grid acceleration

A multi-grid algorithm is employed in order to accelerate the convergence on the fine mesh by damping out the low-frequency error components by means of iterations on coarser meshes [19]. Coarser meshes are generated by eliminating alternate points in each co-ordinate direction. In this way a hierarchy, up to four levels $L = 1, 2, 3, 4$, of grids is created. Within the multi-grid strategy, the following steps are performed. One Runge–Kutta sweep (consisting of a specified number of iterations) is carried on the fine grid according to Equation (32). The solution is restricted from the fine grid (level L) to the next coarse grid (level $L+1$) by the volume-weighted average

$$\mathbf{Q}_0^{L+1} = \frac{1}{\Omega^{L+1}} \sum_{L_{\text{vol}}} [\Omega^L \mathbf{Q}^L]_{L_{\text{vol}}} \tag{34}$$

where the sum is over the eight fine grid control volumes that form the coarse grid control volume. A forcing function $\mathscr{F}$ is defined on the coarse grid by

$$\mathscr{F}^{L+1} = \sum_{L_{\text{vol}}} [\mathscr{R}(\mathbf{Q}^L)]_{L_{\text{vol}}} - \mathscr{R}(\mathbf{Q}_0^{L+1}) \tag{35}$$

which is the difference between the transferred residuals and the coarse grid residuals based on $\mathbf{Q}_0^{L+1}$. A Runge–Kutta sweep is performed on the coarse grid by means of Equation (32) so modified

$$\Omega^{L+1} \frac{\mathrm{d}\mathbf{Q}^{L+1}}{\mathrm{d}t} = \mathscr{T}^{L+1} = \mathscr{R}(\mathbf{Q}^{L+1}) + \mathscr{F}^{L+1} \tag{36}$$

where the forcing function is frozen for a given grid level throughout a multi-grid cycle. The forcing function is constructed so that the solution on a coarse grid is driven by the residuals collected on the next finer mesh (the first iteration is only driven by the collected fine grid residuals). Again the solution and the residuals are restricted to the next coarse grid by calculating the forcing function as

$$\mathscr{F}^{L+1} = \sum_{L_{\text{vol}}} [\mathscr{T}(\mathbf{Q}^L)]_{L_{\text{vol}}} - \mathscr{R}(\mathbf{Q}_0^{L+1}) \tag{37}$$

When the coarsest grid is reached, the corrections are prolonged back to the finger grid by

$$\mathbf{Q}_{\text{new}}^L = \mathbf{Q}^L + p_{L+1}^L (\mathbf{Q}_{\text{new}}^{L+1} - \mathbf{Q}_0^{L+1}) \tag{38}$$

where the prolongation operator p_{L+1}^{L} is a trilinear interpolation operator. The corrections are implicitly smoothed using Equation (33) before updating the finger grid solution. A W-cycle multi-grid algorithm is employed in the present work, where first-order upwind numerical dissipation is used ($\omega = 0$ in Equation (30)) for the coarser grids.

The full multi-grid approach was also tested but with no advantage in terms of computational cost.

The numerical scheme illustrated here may also be extended to time-accurate computations by using a dual time stepping method [5]. In this case, the numerical methods used to accelerate the convergence (local time stepping, smoothing, multi-grid) would be applied for solving the governing equations between two physical time instants.

4.2. Boundary conditions

On the inflow boundary, free-stream values of velocity and scalars are imposed while the pressure is extrapolated from the internal domain. On the outflow boundary, scalars are extrapolated, pressure is fixed and the extrapolated value of velocity is added to a constant chosen in order to satisfy the global conservation of mass at each iteration in the computational domain. On a solid wall, zero-gradient boundary conditions are set for pressure and scalars and the no-slip condition is enforced on the velocity. A 'wall function' approach [12] is used for the turbulent quantities. The 'law of wall' is solved by a Newton–Raphson method in order to obtain the friction velocity u_τ. The values of k and ε in cells immediately adjacent to solid walls are obtained according to

$$k = \frac{u_\tau^2}{\sqrt{c_\mu}}, \qquad \varepsilon = \frac{u_\tau^3}{\chi\zeta} \tag{39}$$

where $\chi = 0.42$ and ζ is the distance from the cell centre to wall. The value of u_τ is also used to fix the value of μ_t at the wall, such that the wall shear stress is equal to ρu_τ^2.

Information coming from adjacent blocks are used as boundary conditions when a multi-block partitioning of complex computational domains is employed.

5. RESULTS

The code was evaluated by simulating a laminar two-dimensional channel and circular duct, laminar and turbulent backward-facing steps and a turbulent diffusion flame, as illustrated in the following sections.

5.1. Two-dimensional channel and circular duct

Solution accuracy and convergence characteristics of the code were initially tested by simulating a laminar flow in a two-dimensional channel and circular duct. The two-dimensional channel is 2 m long and 1 m high, the duct is 2 m long and the diameter is 1 m. A parabolic velocity profile, with a mean value of $U = 0.1$ m s^{-1}, is specified at the entrance. A uniform velocity initial solution is fixed. Reynolds numbers based on 1 m are 50 and 100 for the

two-dimensional and axisymmetric case respectively. The Mach number is 3×10^{-3}. Due to flow symmetry, a grid with only one cell in the azimuthal direction is used. The grid has 80×40 cells in the axial and radial direction respectively and four multi-grid levels were used.

Preliminary experiments studied the influence of β on the convergence of the two-dimensional channel. In Figure 1 the convergence histories for β_0 equal to 0.1, 1, 10 and 100 are shown. Here the logarithm of the L_2-norm of the pressure residual is plotted versus the number of iterations (the first iteration residual is scaled to one). Figure 1 shows that convergence is best for $\beta_0 = 10$. As noted before, when the Reynolds number is low the convergence characteristics improve if β_0 is increased with respect to its optimum inviscid value $\beta_0 = 1$. Actually, as Reynolds number decreases it is necessary that the pressure wave fluctuations in the boundary layer go faster, according to a faster viscosity spreading adjustment. As demonstrated by the case $\beta_0 = 100$, if β_0 becomes too high the convergence slows down due to the increased ill conditions of the inviscid eigenvalues. The benefits of using multi-grid are demonstrated in Figure 2 (however, for higher multi-grid levels the computational cost of a single iteration is larger due to the larger complexity of multi-grid cycles). As a representative quantity to check code accuracy we assumed the relative error of axial pressure gradient with respect to the analytical solution (Poiseuille flow). The small Reynolds number of the test case is consistent with the high turbulent viscosity present in combustion applications. Machine zero accuracy is achieved for all the cases. The solutions on the two-dimensional 80×40 grid were found to be β-independent with respect to the pressure error. Starting from the 80×40 grid, in the multi-grid strategy 40×20, 20×10 and 10×5 grids are generated. Calculations for two-dimensional channel and circular duct were performed on the four grids with $\beta_0 = 10$ and using the coarser grids for the multi-grid cycles. Table I illustrates the results of our calculations and those of Cabuk *et al.* [20], where a preconditioning method is also employed. Table I shows the accuracy gain with decreasing grid size. Grid independency is achieved before for the circular duct.

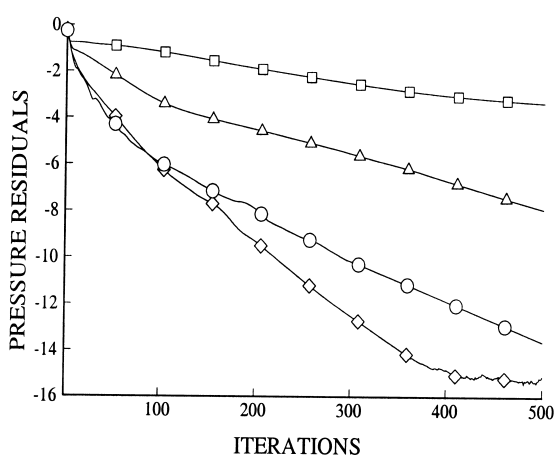

Figure 1. Two-dimensional channel, 80×40 grid. Pressure residual versus number of iterations: □, $\beta_0 = 0.1$; △, $\beta_0 = 1$; ◇, $\beta_0 = 10$; ○, $\beta_0 = 100$.

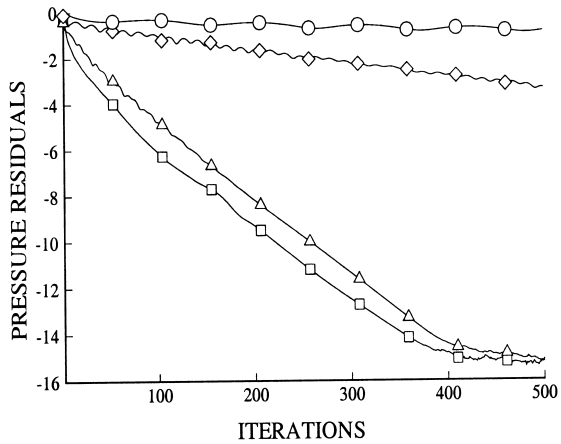

Figure 2. Two-dimensional channel, 80×40 grid, $\beta_0 = 10$. Pressure residual versus number of iterations: □, four multi-grid levels; △, three multi-grid levels; ◇, two multi-grid levels; ○, one multi-grid level.

Table I. Two-dimensional channel and circular duct.

Grids	Two-dimensional channel (%)		Circular duct (%)	
	A	B	A	B
10×5	2.8	5.1	0.4	15.7
20×10	0.6	0.9	0.27	3.1
40×20	0.16	0.15	0.252	0.4
80×40	0.04	0.02	0.250	—

Pressure gradient relative errors with respect to analytical solution for $\beta_0 = 10$: A, present calculations; B, Cabuk *et al.* [20].

5.2. Laminar backward-facing step

Another test case studied is that of a two-dimensional laminar flow between a flat plate and a backward-facing step. The problem has been experimentally investigated by Armaly *et al.* [21]. The geometry is shown in Figure 3, where $H = Y = 0.5$ cm, $s = 4H$ and $L = 30H$. The flow reattaches at distance x_1 downstream the step. From Armaly's experiments, when $Re < 800$ (Re being based on the hydraulic diameter of $2H$) the flow is laminar and no three-dimensional effect is present. Furthermore, an additional recirculation flow region appears on the upper flat plat when $Re > 400$. This zone extends downstream of the step between x_2 and x_3.

In our calculations a parabolic velocity profile, with a mean value $U = 1$ m s^{-1}, is specified at the entrance (the corresponding Mach number is 3×10^{-3}). A two-block mesh simulates the inlet channel. The meshes for block 1 and block 2 have 16×32 and 120×64 cells respectively

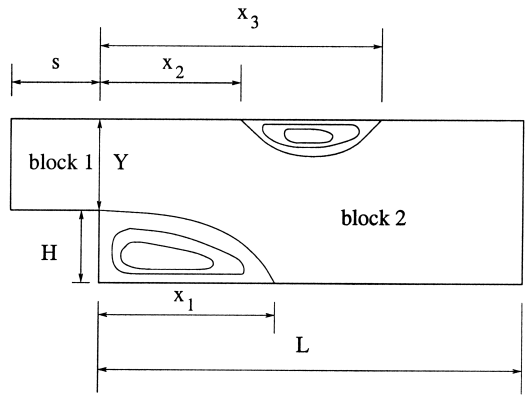

Figure 3. Geometry of backward-facing step.

and three levels of multi-grid are employed. Calculations were performed at Re equal to 100, 152, 303, 389, 452, 500, 600, 700 and 800. The values of β_0 ranged from $\beta_0 = 0.01$ at $Re = 800$ to $\beta_0 = 10$ at $Re = 100$. No convergence was achieved at higher Re if $\beta_0 > 0.01$, showing that the presence of large recirculation zones requires the propagation speed of pressure waves to be slow. The reattachment distances x_1/H and x_3/H and the separation distance x_2/H calculated for different Re are shown in Figure 4, where the experiments of Armaly and the numerical results of Cabuk *et al.* [20], Kim and Moin [22], Rogers and Kwak [23] are also reported. There is good agreement between our results and those of the other authors.

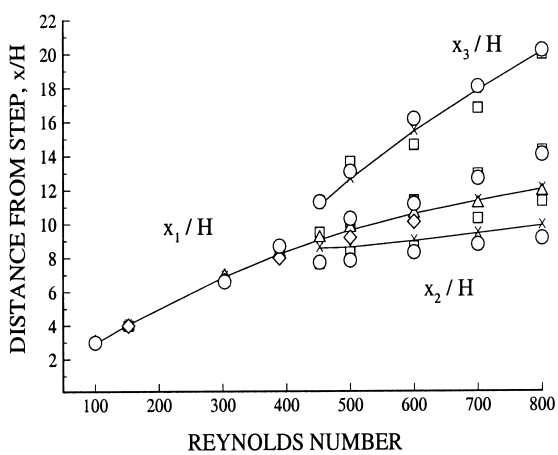

Figure 4. Laminar backward-facing step. Separation (x_1, x_2) and reattachment (x_3) points at different Re: —, present calculations; □, Armaly *et al.* [21]; △, Kim and Moin [22]; ◇, Cabuk *et al.* [20]; ○, Rogers and Kwak [23].

5.3. Turbulent backward-facing step

The geometry of this two-dimensional planer turbulent test case is that of Figure 2, where $H = 1.27$ cm, $Y = 8H$, $s = 4H$ and $L = 30H$. In the experiments performed by Driver and Seegmiller [24], mean velocity and turbulent kinetic energy transversal profiles have been measured at different axial positions. The profiles at $4H$ upstream of the step have been used as inlet profiles in our computation. The inlet values of ε were calculated through the relation

$$\varepsilon = \frac{k^{3/2}}{0.3 \cdot Y} \tag{40}$$

The Re based on the inlet mean velocity $U = 44.2$ m s^{-1} is 3×10^5 and the flow is fully turbulent. The value $\beta_0 = 1$ was used. Blocks 1 and 2 have 16×64 and 96×72 cells respectively.

The standard k–ε model predicts a reattachment length of $x_1/H \simeq 5.1$, while in the experiments $x_1/H \simeq 6.2$. Therefore, the standard k–ε model underpredicts the experimental reattachment length. Figures 5 and 6 show the transversal profiles of the axial velocity and turbulent kinetic energy at different axial positions, x/H. In all cases, agreement between predicted and experimental profiles is good.

5.4. Coaxial jet flame with flame-holder

This test case is based on an experimental axisymmetric configuration tested by Correa and Gulati [25]. The three-block computational domain and the streamline pattern are shown in Figure 7. The combustor is a 15×15 cm square section wind tunnel (simulated as axisymmetric) with a 3.18 mm in diameter cylindrical fuel nozzle located along the axis. A 38.1-mm

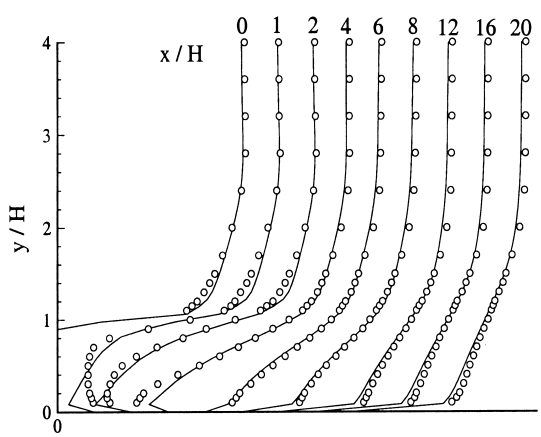

Figure 5. Turbulent backward-facing step. Velocity profiles at different distances x/H from the step: —, present calculation; ○, Driver and Seegmiller [24].

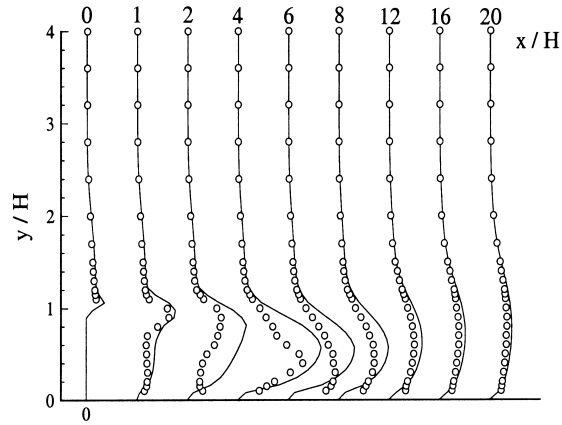

Figure 6. Turbulent backward-facing step. Turbulent kinetic energy at different distances x/H from the step: —, present calculation; ○, Driver and Seegmiller [24].

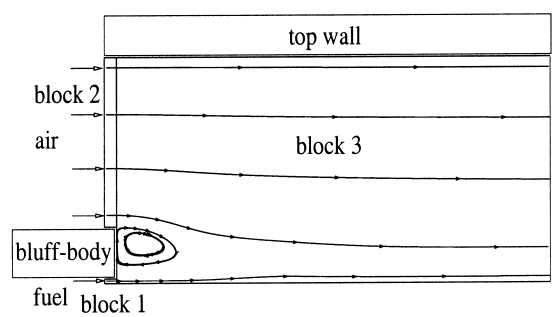

Figure 7. Geometry and streamlines of coaxial jet flame.

diameter axisymmetric bluff body flame-holder surrounds the fuel nozzle in order to create a recirculation zone. The fuel molar fraction composition is 27.5 per cent CO, 32.3 per cent H_2; 40.2 per cent N_2. This density is evaluated by the thermochemical equilibrium relation (14), where $N = 15$. The corresponding polynomial fit $F(f)$ is shown in Figure 8. The maximum density variation is $\rho(f_{st})/\rho(0)$, where $f_{st} = 0.35$ is the mixture fraction stochiometric value. The fuel and air velocities are 80 and 6.5 m s^{-1}, respectively. Pressure is 101 000 Pa and fuel and air temperatures are 300 K each. Uniform inlet velocity profiles were used for both fuel and air. The inlet value of k was $0.005 \cdot U^2$ and ε was given by Equation (40). An axisymmetric grid with 5504 cells and a spread angle of 10° was used. Density relaxation was necessary to achieve the steady solution because of the strong density variation (see Figure 8) especially

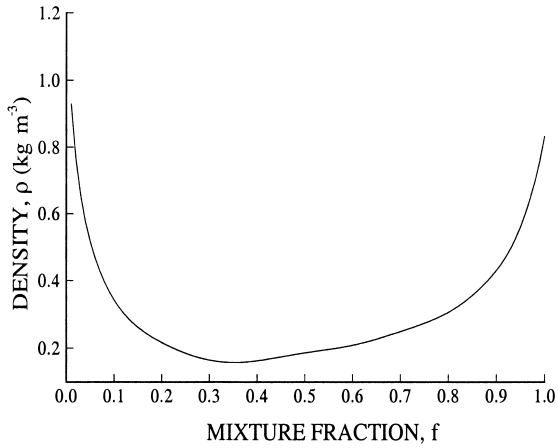

Figure 8. Coaxial jet flame. Thermochemical equilibrium polynomial fit for mixture density.

during the first iterations. The density at the $n+1$ time step is relaxed according to the formula

$$\rho_{\text{new}} = \alpha\rho^n + (1-\alpha)\rho^{n+1} \tag{41}$$

where the relaxation factor $\alpha = 0.001$ is employed.

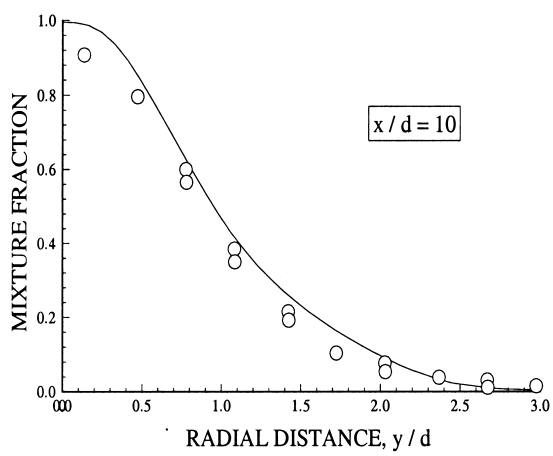

Figure 9. Coaxial jet flame. Mixture fraction $\tilde{f}$ radial profile at distance $x/d = 10$ from the bluff body: —, present calculation; ○, Correa and Gulati [25].

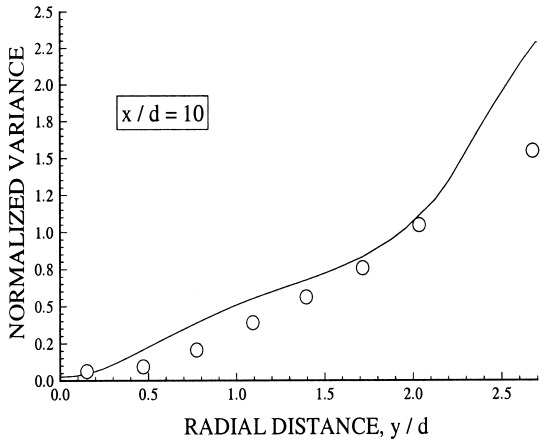

Figure 10. Coaxial jet flame. Normalized mixture fraction variance $\sqrt{\widetilde{f''^2}}/\tilde{f}$ at distance $x/d = 10$ from the bluff body: —, present calculation; ○, Correa and Gulati [25].

The radial profiles of mixture fraction $\tilde{f}$ and of its normalized variance $\sqrt{\widetilde{f''^2}}/\tilde{f}$ at the axial station $x/d = 10$ (where d is the diameter of the fuel jet) are shown in Figures 9 and 10. Here also the experiments of Correa are reported. In Figure 11 the radial profile of $\tilde{f}$ at $x/d = 20$ is shown. Comparison between predictions and experiments is satisfactory under the approximation of thermochemical equilibrium.

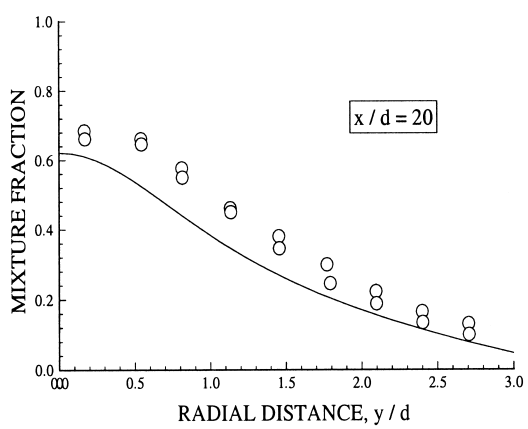

Figure 11. Coaxial jet flame. Mixture fraction $\tilde{f}$ radial profile at distance $x/d = 20$ from the bluff body: —, present calculation; ○, Correa and Gulati [25].

6. CONCLUSIONS

A numerical code for low-speed turbulent flows has been presented. A preconditioning method is applied to a density based formulation suitable for both non-reactive flows and non-premixed combustion flows. The preconditioning allows for retaining all the numerical characteristics of density based codes and overcoming their difficulties when simulating low-speed flows. A MUSCL spatial discretization and a multi-grid technique have been developed for the preconditioned system. This solver extends explicit CFD solutions to non-reactive and reactive flows with very low Mach numbers, down to $\mathcal{O}(10^{-3})$. The method has been used to successfully simulate laminar and turbulent cold flows as well as a combustion flow characterized by large density fluctuations. The numerical results are in agreement with experiments and with results obtained by other authors.

ACKNOWLEDGMENTS

This work has been financially supported by the Sardinian Regional Authority and by EC under the TANIT Project ESPRIT-HPCN 8835.

REFERENCES

1. Libby PA, Williams FA. Fundamental aspects. In *Turbulent Reacting Flows*, *Topics in Applied Physics*, vol. 44, Libby PA, Williams FA (eds). Springer: New York, 1980; 1–43.
2. Chorin AJ. Numerical solution of Navier–Stokes equations. *Mathematics of Computation* 1968; **22**: 745–762.
3. Patankar SV. *Numerical Heat Transfer and Fluid Flow*. Hemisphere Publishing: New York, 1980.
4. Chorin AJ. A numerical method for solving incompressible viscous flow problems. *Journal of Computational Physics* 1967; **2**: 12–26.
5. Merkle CL, Choi Y-H. Computation of low-speed compressible flows with time-marching procedures. *International Journal for Numerical Methods in Engineering* 1988; **25**: 293–311.
6. Turkel E. Preconditioning methods for solving the incompressible and low speed compressible equations. *Journal of Computational Physics* 1987; **72**: 277–298.
7. Rogers SE, Kwack D. Steady and unsteady solutions of the incompressible Navier–Stokes equations. *AIAA Journal* 1991; **29**: 603–610.
8. van Leer B, Lee WT, Roe PL. Characteristic time stepping or local preconditioning of the Euler equations. AIAA Paper 91-1552, 1991.
9. Choi Y-H, Merkle CL. The application of preconditioning in viscous flows. *Journal of Computational Physics* 1993; **105**: 207–223.
10. Shuen J-S, Chen K-H, Choi Y. A coupled implicit method for chemical non-equilibrium flows at all speeds. *Journal of Computational Physics* 1993; **106**: 306–318.
11. Dailey L, Pletcher R. Evaluation of multigrid acceleration for preconditioned time-accurate Navier–Stokes algorithms. AIAA Paper 95-1668, 1995.
12. Launder BE, Spalding DB. The numerical computation of turbulent flows. *Computer Methods in Applied Mechanics and Engineering* 1974; **3**: 269–289.
13. Bilger RW. Turbulent flows with nonpremixed reactans. In *Turbulent Reacting Flows*, *Topics in Applied Physics*, vol. 44, Libby PA, Williams FA (eds). Springer: New York, 1980; 65–113.
14. Gordon S, McBride B. Computer program for calculation of complex chemical equilibrium compositions. NASA SP-273, 1971.
15. Girimaji SS. Assumed β-PDF model for turbulent mixing validation and extension to multiple scalar mixing. *Combustion Sciences and Technology* 1991; **78**: 177–196.
16. Abramowitz M, Stegun IA. *Handbook of Mathematical Functions*. National Bureau of Standards: Washington, DC, 1964.
17. Roe PL. Approximate Riemann solver, parameter vectors, and difference schemes. *Journal of Computational Physics* 1981; **43**: 357–372.

18. van Leer B. Towards the ultimate conservative difference scheme V. A second-order sequel to Godunov's method. *Journal of Computational Physics* 1979; **32**: 101–136.
19. Martinelli L. Calculations of viscous flows with a multigrid method. PhD thesis, MAE Department, Princeton University, Princeton, NJ, 1987.
20. Cabuk H, Sung C-H, Modi V. Explicit Runge–Kutta method for three-dimensional internal incompressible flows. *AIAA Journal* 1992; **30**: 2024–2031.
21. Armaly B, Durst F, Pereira J, Schonung B. Experimental and theoretical investigation of backward-facing step flow. *Journal of Fluid Mechanics* 1983; **127**: 473–496.
22. Kim J, Moin P. Application of a frctional-step method of incompressible Navier–Stokes equations. *Journal of Computational Physics* 1985; **59**: 308–323.
23. Rogers SE, Kwak D. An upwind differencing scheme for the time-accurate incompressible Navier–Stokes equations. AIAA Paper 88-2583, 1988.
24. Driver DM, Seegmiller HL. Features of a reattaching turbulent shear layer in divergent channel flow. *AIAA Journal* 1985; **23**: 163–171.
25. Correa SM, Gulati A. Measurements and modeling of a bluff body stabilized fame. *Combustion and Flame* 1992; **89**: 195–213.

